

CNN-based Visual Ego-Motion Estimation for Fast MAV Maneuvers

Yingfu Xu and Guido C. H. E. de Croon

Abstract—In the field of visual ego-motion estimation for Micro Air Vehicles (MAVs), fast maneuvers stay challenging mainly because of the big visual disparity and motion blur. In the pursuit of higher robustness, we study convolutional neural networks (CNNs) that predict the relative pose between subsequent images from a fast-moving monocular camera facing a planar scene. Aided by the Inertial Measurement Unit (IMU), we mainly focus on the translational motion. The networks we study have similar small model sizes (around 1.35MB) and high inference speeds (around 100Hz on a mobile GPU). Images for training and testing have realistic motion blur. Departing from a network framework that iteratively warps the first image to match the second with cascaded network blocks, we study different network architectures and training strategies. Simulated datasets and MAV flight datasets are used for evaluation. The proposed setup shows better accuracy over existing networks and traditional feature-point-based methods during fast maneuvers. Moreover, self-supervised learning outperforms supervised learning. The code developed for this paper will be open-source upon publication at <https://github.com/tudel1ft/>.

I. INTRODUCTION

Indoor flight of Micro Air Vehicles (MAVs) is an attractive but challenging task. Towards the goal of autonomy, robust state estimation is one of the most essential modules of the MAV’s flight control system. A camera captures rich information in a big field of view. Since being small and power-efficient, it is an ideal onboard sensor [1]. Its combination with the high-sample-frequency IMU is not only suitable for environment perception but also for real-time ego-motion estimation. Visual [2], [3] and visual-inertial [4], [5], [6], [7], [8] odometry (VO/VIO) systems contribute to MAVs’ autonomy in generic environments by achieving real-time efficiency on onboard processors with decent accuracy.

Being constrained by the limited battery life, increasing flight speed is a direct way to enlarge an MAV’s operation range and efficiency. However, it also introduces challenges for perception, and notably VO/VIO. Detection and tracking of handcrafted interest-point-based features [9], [10], [11] is the standard in state-of-the-art VIO systems [6], [7], [8]. However, such systems lack robustness in the presence of motion blur occurring during fast maneuvers.

Robust Visual Inertial Odometry (ROVIO) [5] directly uses photometric errors of multilevel image patches around FAST feature points [10] to be more robust against image blur than point features, partly because the texture of the tracked image patch is taken into account. However, Foehn *et al.* point out that at larger speeds the state estimate of

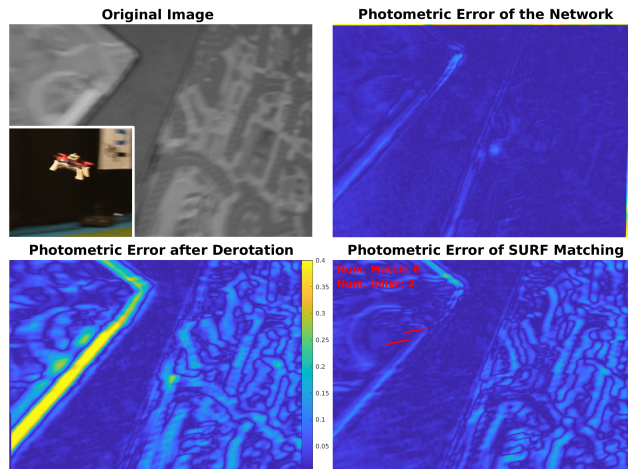


Fig. 1. We study CNNs for visual ego-motion estimation, using blurry gray-scale images captured by the downward-facing camera of fast-moving MAVs. The derotated image pair has big photometric errors. After being warped by the network’s prediction of the relative pose, only small photometric errors can be found around edges. The proposed networks better cope with fast motion than traditional feature-based methods.

ROVIO suffers from drift [12]. When the speed gets larger, feature points can move out of the camera’s field of view sooner. We believe that the bigger visual disparity between images and the consequent lower number of frames in which features can be tracked is another adverse condition besides motion blur. Since ROVIO takes features’ 3-dimensional (3-d) positions as states of an extended Kalman filter (EKF), having fewer visual observations decreases the accuracy. Other VIO systems such as [4], [6] that estimate feature positions by multiple observations can also suffer from high-speed motion [13].

CNNs are state of the art in many computer vision tasks and are promising for VO as well. Various networks have been proposed to estimate the pose change (rotation and translation) between two or more subsequent views. There are not only supervised pose networks trained by limited ground truth [14], [15], [16] but also self-supervised ones trained together with other networks including a depth estimation network [17], [18], [19], [20], [21]. These networks obtain highly accurate performances rivaling VO [3] with a traditional vision method [11] on the KITTI dataset [22].

There are also pose networks considering the application to an MAV’s ego-motion estimation. For example, in [16], a recurrent CNN is trained on the EuRoC MAV dataset [23] to regress the 6 degree-of-freedom motion. The network manages to learn the more complex (compared with a car) MAV’s dynamics but the accuracy is limited by the

The authors are with the Micro Air Vehicle Laboratory, Faculty of Aerospace Engineering, Delft University of Technology, The Netherlands. (email: y.xu-6@tudelft.nl; G.C.H.E.deCroon@tudelft.nl).

small amount of training data. Differently, PRGFlow [24] focuses on the essential function of estimating the 3-d translational velocity of the MAV with a downward-facing camera, assuming a planar ground. Aided by the attitude estimated using IMU measurements, via image warping, the task is simplified to the pixel-level similarity transformation estimation. Although PRGFlow thoroughly studied CNN-based ego-motion estimation, the focus is on the low-speed flight (about 0.5m/s on average), with blur lacking from the artificially generated training images.

Hence, it is currently still an open question of how good CNNs perform during fast maneuvers. To gain insight into this matter, in this article we study networks predicting 3-d relative translation of MAVs in fast maneuvers with a downward-facing camera. The networks are trained and tested on images with significant motion blur and big visual disparities. Our main contributions are that we: (1) Extend and further improve the performance of the network framework proposed in [24] for fast maneuvers, and (2) Investigate how well the networks can deal with faster maneuvers in comparison with traditional feature-point-based methods. According to our knowledge, this is the first paper showing networks' superior performance in fast maneuvers when traditional feature-point-based methods have high failure rates.

The remainder of the article is organized as follows. First, we introduce our setups of network architectures, image datasets, and training strategies in Section II. Then, to maximize the network's potential, we compare a variety of networks under the constraints of model size and inference speed and perform both supervised and self-supervised learning in Section III. Last in Section IV, in the comparison with feature-based methods, we study how motion blur and visual disparity affect the network's performance and evaluate it by flight datasets containing fast maneuvers.

II. METHODOLOGY

A. Homography Transformation

As shown in Eq. 1, for a fixed point laying on a plane observed by two cameras, it has been proven in [25] that the projective coordinates x_1 , x_2 of the same point in the camera frames are related by the homography matrix H that depends only on the 6-d relative pose of the cameras and the unit normal vector of the plane n . R denotes the rotation matrix between the camera frames and t denotes the translation vector expressed in the second camera's frame pointing from the second camera to the first one. The scalar d is the distance from the first camera to the plane.

$$x_2 = Hx_1, H = R + \frac{tn^T}{d} \quad (1)$$

Here we define the coordinate system whose x -axis points to the north, y -axis to the east, and z -axis to the gravity direction as the world frame. The plane that the downward-facing camera observes is assumed to be orthogonal to the gravity vector. Then the information remaining unknown in the homography matrix is the ratio of the translation vector

to the first camera's distance to the plane. Here we refer to it as the distance-scaled relative translation vector. This vector together with the flight height that is available from a downward-facing rangefinder can determine the metric average translational velocity of the MAV during the camera's sample interval. Here we refer to it as the distance-scaled translational velocity vector.

Sanket *et al.* [24] warp both the images to make the image planes parallel to the ground using the attitude from the IMU. The distance-scaled relative translation then can be determined by the similarity transformation between the image pair. Networks are trained to predict the 3 parameters (2-d translation, zoom-in/out) reflecting the relative position of pixels. However, when the roll or pitch angle of the MAV is big, which is often the case in fast maneuvers, the camera would have big tilt angles relative to the plane's normal vector. So warping the image pair like [24] can cause big black boundaries and thus lose many pixels. It then requires pre-processing moving the pixels back inside the image frame and the corresponding post-processing for calculating the pose from the similarity transformation. For faster network inference, we train the networks to predict the distance-scaled relative translation expressed in the camera frame directly from images that have (non-zero) tilt angles. So only one image is required to be warped by the relative rotation between the images. Directly regressing to pose makes the network learn the intrinsics of the camera. For the tilt angles, they are available from IMU but we additionally explore to train networks predicting them in subsection III-D.

B. Cascaded Network Blocks Connected by Image Warping

Sanket *et al.* adopt the inverse compositional spatial transformer networks (ICSTN) [26] as the framework of their networks [24]. The ICSTN has multiple network blocks that predict the image deformation that can benefit the final goal. Based on the homography transformation, a new image can be synthesized by warping the original image using the method proposed in [27]. As shown in Fig. 2, a network block is made up of multiple convolutional layers followed by a fully-connected layer regressing the translation. With multiple cascaded network blocks, each block can take the concatenated image 1 and image 2 that is warped by the newest pose prediction as input and combine its output into the pose prediction. As the pose prediction is refined by more blocks, there is less relative motion between the concatenated images. Each block predicts a part of the total

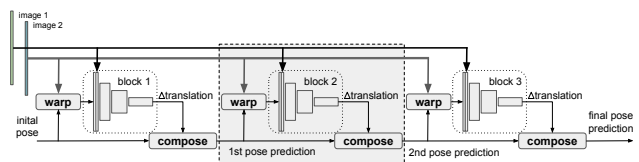


Fig. 2. An ICSTN-based network with 3 blocks for relative pose prediction. The dashed line frame indicates the basic functional unit that can be sequentially stacked one or multiple times. The dotted frame indicates a network block that takes (downsampled) concatenated images as input and predicts the 3-d distance-scaled relative translation.

relative translation, making the problem more tractable. The network can also make use of an initial guess of the relative pose, which may be available from the IMU integration or the MAV’s dynamic model. PRGFlow has compared network architectures inside one block. Focusing on fast maneuvers, we study higher-level architectures applying to the pyramidal images and feature maps to enlarge the receptive field which is important for dealing with the big disparity.

The loss functions of the networks are the mean of the Charbonnie [28] loss of the predicted 3-d translation’s error in supervised learning and the mean of the Charbonnie loss of the valid pixels’ photometric error in self-supervised learning. Except for subsection V-B, the pose at the exposure starting step of an image is used as the ground truth in supervised learning. For data augmentation, we feed the network with image pairs concatenated in both orders to perform bidirectional training.

We implement the networks in Python 3.6.9 with the Pytorch [29] 1.1.0 library. During the training of 25 epochs, we use the Adam optimizer [30] with $\beta = (0.9, 0.999)$. The batch size is 16. The initial learning rate is 0.0002 and it is divided by 2 after 5, 10, 15, and 20 epochs. The weights of convolutional layers are initialized by Glorot initialization [31] with a gain of 1. The weights of fully-connected layers are initialized by the (Pytorch default) uniform distribution $\mathcal{U}(-\sqrt{k}, \sqrt{k})$ where k is the multiplicative inverse of the number of input features. The inference speeds are indicated in frames per second (FPS) of one network running on an NVIDIA Jetson TX2 with Ubuntu 18.04.3 LTS, Cuda V10.0.326. The TX2’s MAXP_CORE_ARM power mode shows the highest inference speed of our implementation.

C. Dataset Generation

We use the Microsoft COCO dataset [32] as the source of a large variety of textures to generate a big number of image pairs thanks to the homography transformation. A source image is treated as a plane above which a simulated camera is moving. For one plane, one image pair is generated. Costante *et al.* and Kendall *et al.* test their pose estimation networks with respectively artificial Gaussian blur [14] and motion blur [33] added to images. Their blur is uniform over the whole image and thus not ego-motion-related. In order to obtain realistic blur that is caused by the camera’s motion within the exposure duration, we simulate a moving camera whose time step for the kinetic integration is 0.1 millisecond (ms) and the exposure duration is 10 ms. In each integration step during the exposure, an image is sampled from the homography transformation of the plane. The blurry image



Fig. 3. A blurry image pair in the dataset. Starting from the left, the images are respectively the first image, the derotated second image, and the second image.

is the average of the 100 sampled images. The poses of both the exposure starting step and ending step of an image are recorded. We set the frame rate at 30Hz to simulate a low-cost global shutter camera. The images are in grayscale with the resolution of 320×224 pixels. The intrinsics of the simulated camera are $f_x = 160$, $f_y = 160$, $c_x = 160$, $c_y = 112$.

The initial poses of the integration uniformly distribute within a normal quadrotor MAV’s flight envelope. The uniformly randomly generated translational velocity and rotational velocity stay constant during the kinetic integration. The camera’s distance-scaled translational velocity vector’s components of the x -axis and y -axis of the world frame range from -7.5 to 7.5 . The range of the component of the z -axis is from -3.75 to 3.75 . Angular velocity vector’s components of the x -axis and y -axis of the camera frame range from -180 to 180 degrees per second. The range of the component of the z -axis is from -90 to 90 degrees per second. Initial pitch and roll angles range from -25 to 25 degrees. Since we record the poses at the start and the end of exposure duration, the motion flow that causes blur can be calculated. Over the dataset, the average motion flow of all the pixels in an image has mean values of 6.6 and 6.2 pixels in the x -axis and y -axis, respectively. The maximum motion flow of all the pixels in an image has mean values of 13.4 (x -axis) and 11.9 (y -axis) pixels. The above data shows that our dataset involves a big range of motion and significant motion blur. After removing hundreds of images with little texture, there are 82,172 training samples, 9,948 validation samples (for validating the model after each epoch during training), and 30,565 testing samples.

III. NETWORKS

A. ICSTN-based Networks

In Table I, we compare networks with different numbers of blocks. All blocks have identical architecture. “Num. Conv.” is the abbreviation of the number of convolutional layers. “RF” denotes the receptive field of the fully-connected layer’s input. We call the final prediction error the end-point error (EPE). The predicted translation is rotated into the world frame to calculate the 3-d EPE vector. EPE’s standard deviation can reflect how noisy the prediction is but it is sensitive to outliers that can be caused by image pairs lacking texture or having duplicate textures. So we use a local outlier rejection function of MATLAB to remove outliers and keep the characteristic of local distribution (shown in Subsection V-B). After respectively ascendingly sorted by the corresponded ground truth along each axis, the EPEs whose absolute values are more than 3 scaled median absolute deviations in a local window of size 1000 are rejected. A prediction is considered an outlier if in any of the axes it is considered an outlier. The 3 values inside the bracket separated by commas correspond to the data in the x -axis, y -axis, and z -axis. The medians of EPE’s absolute values are calculated from all (including outliers) the data. We list the kernel sizes and the strides of the first and second

TABLE I
ICSTN-BASED NETWORKS WITH DIFFERENT NUMBERS OF BLOCKS

Network	Num. Blocks	Num. Conv./ Kernel/ Stride	Num. Params	FPS	RF	Inlier Rate(%)	EPE's Standard Deviations (1e-3) (end-point loss / multi-stage losses)	Medians of EPE's Absolute Values (1e-3) (end-point loss / multi-stage losses)
[17]	1	8/ 7,5/ 2,2	1.583M	215	263	90.14	(13.44,13.88,19.23)	(7.83,8.11,11.93)
[34]	1	18/ 3,3/ 2,2	1.441M	105	759	91.77	(6.70,6.94,9.63)	(3.85,4.03,6.12)
[35]	1	21/ 3,3/ 2,2	1.477M	103	975	92.35	(7.32,7.58,10.57)	(4.33,4.48,6.66)
(ours)	2	9/ 7,5/ 2,2	1.385M	104	647	89.92	(3.35,3.30,3.91) / (2.71,2.64,3.28)	(1.89,1.89,2.61) / (1.49,1.49,2.18)
(ours)	3	5/ 7,5/ 2,2	1.367M	101	71	87.59	(3.33,3.15,4.29) / (2.28,2.22,3.08)	(1.91,1.83,2.90) / (1.24,1.22,2.11)
(ours)	3	5/ 7,5/ 4,2	1.252M	101	135	92.18	(2.06,2.05,2.90)	(1.16,1.13,2.00)
(ours)	4	3/ 7,5/ 4,4	1.421M	95	55	85.48	(3.58,3.51,4.75) / (2.20,2.19,3.06)	(2.20,2.20,3.20) / (1.28,1.26,2.13)
(ours)	4	3/ 9,5/ 8,4	1.276M	95	105	87.35	(2.10,2.09,3.01)	(1.25,1.22,2.09)

TABLE II
ICSTN-BASED NETWORKS USING PYRAMIDAL IMAGES OR FEATURE MAPS

Num. Pyramid	Num. Layers/ Kernel/ Stride	Num. Params	FPS (intrpl. / avg. pooling)	Receptive Field	EPE's Standard Deviations (1e-3) (intrpl. / avg. pooling)
3	3/ 7,5/ 2,2; 4/ 7,5/ 2,2; 5/ 7,5/ 2,2	1.388M	103 / 108	23×4; 39×2; 71	(2.13,2.05,2.93) / (2.11,2.09,2.91)
3	3/ 7,5/ 4,2; 4/ 7,5/ 4,2; 5/ 7,5/ 4,2	1.272M	104 / 111	39×4; 71×2; 135	(2.11,2.09,2.94) / (2.09,2.06,2.94)
3	4/ 7,5/ 2,2; 4/ 7,5/ 4,2; 4/ 7,5/ 4,4	1.316M	104 / 109	39×4; 71×2; 119	(2.07,2.06,2.93) / (2.07,2.07,2.90)
4	2/ 7,5/ 2,2; 2/ 7,5/ 4,2; 3/ 7,5/ 4,2; 3/ 7,5/ 4,4	1.386M	93 / 98	15×8; 23×4; 39×2; 55	(2.03,2.02,2.87) / (2.02,2.02, 2.85)
3	[FPE: 3/ 7,5/ 2,2] + [2; 3; 4]	1.455M	100	71; 71; 71	(2.18,2.12,3.12)
3	[FPE: 3/ 7,5/ 4,2] + [2; 3; 4]	1.340M	100	135; 135; 135	(2.00,1.97,3.08)

convolutional layers of a block in the 3rd column. Deeper layers have the kernel sizes of 3 and strides of 2 or 1.

In Table I, first, we compared the networks with a single block. The 1st network is the pose estimation network proposed in [17]. The 2nd and 3rd networks are deeper. We respectively use skip connections [34], [35] for better performance. From the first 3 rows of Table I, we notice that deeper networks with smaller model sizes have higher accuracy but slower speed. And the 2nd network with 18 layers and densely connected architecture has the highest accuracy. In the case of multiple blocks, for each block, there is an image warping operation that has unneglectable time consuming. Since we require the networks' inference speed to be around 100Hz, the total number of layers in the whole network decreases when the number of blocks increases. The accuracy gets worse when there are more than 3 blocks mainly because the blocks are too shallow and the total capacity of the whole network decreases. As shown by the 6th and 8th networks, bigger strides lead to smaller resolution of the last feature map and thus fewer parameters in the fully-connected layer. Besides, it increases the receptive field. Since our dataset has samples with big motion, the bigger receptive field can capture more feature correspondence and improve the accuracy.

For the networks with multiple blocks, instead of only using the loss of the final prediction (end-point loss) in training like PRGFlow, we weighted sum the losses of every prediction after every block (multi-stage losses) for backpropagation. The loss weight distributions of blocks are respectively [0.3,0.7], [0.2,0.3,0.5], and [0.1,0.2,0.3,0.4] for networks with 2, 3, and 4 blocks. The accuracy is compared by the 4th, 5th, and 7th networks of Table I. Multi-stage losses produce higher accuracy. For the 6th and 8th networks, we only show the results of multi-stage losses. From now on,

all the networks in the article are trained with multi-stage losses.

B. Pyramidal Images and Feature Maps in ICSTN

From Table I, we find that a bigger receptive field can benefit accuracy. When the kernel size and stride keep the same, another way to increase the receptive field is using pyramidal images. In Table II, we show networks using pyramidal images or feature maps with lower resolution. The downsampled image at each pyramid level has half the size of the image at the adjacent lower level. So the lowest-resolution image of the network that has 4 pyramids has one-eighth the width and height of the original image. The number of network blocks is the same as the number of pyramids. The first pose prediction block uses the images at the highest pyramid level with the lowest resolution. The predicted pose is used to warp the original image. Then the warped image is downsampled to the next lower pyramid level and input to the next network block. For image downsampling, we compared bilinear image interpolation and average pooling. They have similar accuracy, but average pooling is faster in our Pytorch implementation.

Because the EPE's standard deviation can reflect the accuracy of the networks, so in this table we only show the standard deviation. Comparing the 1st network of Table II with the 5th one in Table I, with the same kernel size and stride, the pyramidal network that has fewer layers achieves higher inference speed and accuracy, thanks to the bigger receptive field of the first two blocks. Comparing the 2nd network of Table II with the 6th network of Table I, the pyramidal network has slightly lower accuracy. We think it is because when the network already has a big receptive field, the pyramidal version receives less information because of the downsampling. The 8th network of Table I has a big

TABLE III
COMPARISON BETWEEN SUPERVISED AND SELF-SUPERVISED LEARNING

Networks	Inlier Rate(%) (supervised / self-supervised)	EPE's Standard Deviations (1e-4) (supervised / self-supervised)	Medians of EPE's Absolute Values (1e-4) (supervised / self-supervised)
Table I 6	92.18 / 91.41	(20.62, 20.46, 28.99) / (19.16, 19.29, 28.36)	(11.62, 11.29, 20.01) / (10.71, 10.60, 19.54)
Table I 6*	75.20 / 70.84	(5.30, 4.95, 7.04) / (4.16, 3.82, 5.54)	(3.15, 3.15, 4.55) / (2.40, 2.15, 3.47)
Table II 3(p)*	73.20 / 69.91	(5.49, 4.93, 7.02) / (4.20, 3.79, 5.52)	(3.08, 2.91, 4.42) / (2.36, 2.16, 3.47)
Table II 4(i)*	71.43 / 67.29	(4.49, 4.23, 5.94) / (3.08, 2.89, 3.90)	(2.82, 2.64, 3.93) / (1.91, 1.80, 2.63)

receptive field. Also with 4 blocks, the 4th network of Table II has decreasing receptive fields with the increasing of image resolution. Although 3 blocks out of 4 have smaller receptive fields than the 8th network of Table I, this 4-stage coarse-to-fine refinement gets better accuracy. The 2nd and 3rd network of Table II have the same total number of layers. The 3rd one having a deeper block at the lowest resolution achieves slightly higher accuracy.

The pyramidal feature maps network is based on the feature pyramid extractor (FPE) inspired by the PWC-Net [36]. The results are shown in the last 2 rows of Table II. The general principle is extracting multiple feature maps at different resolutions (pyramid levels) of each image respectively by the same convolutional feature extractor network. One of the feature maps is warped and then concatenated along the channel dimension with the other feature map of the same size. The concatenated feature maps are the input of the pose prediction blocks. The networks we design have 3 levels of pyramidal feature maps and 3 pose prediction blocks that have 2, 3, and 4 convolutional layers respectively. The FPE network at the last row of Table III has the highest accuracy in the x -axis and y -axis but the error in the z -axis is relatively bigger. We notice that for all the networks in this article the z -axis has less accurate predictions. This is also the case for most networks in [24]. It is possible that a standard CNN's ability to estimate scale variations is fundamentally limited (cf. [37], [38]). A deeper analysis of this issue is required.

C. Self-Supervised Learning

Self-supervised Learning is based on the photometric error between the image warped by the predicted translation and the other image. We use a mask to not count the photometric errors of the pixels whose locations to interpolate lie outside the image frame.

By the results shown in the 1st row of Table III (note that the size factor of data in the column title of this table is 1e-4 instead of 1e-3 in previous tables), we notice that self-supervised learning gets better accuracy than supervised learning only with a basic Charbonnie loss. The reason behind it worth further studying. For now, we think it is mainly because the target relative poses used in supervised learning are calculated from the poses at the starting time points of the images' exposure. While the simulated camera keeps moving within the exposure duration, motion blur appears and the image gets a different appearance from the start of exposure, and thus there will be small photometric errors between the images warped by the target relative pose.

This means the network is learning to regress to a target not perfectly matching the feature correspondences. This mismatch can "confuse" the network. While in the case of self-supervised learning, the network tries to minimize the photometric error affected by the blur and is more likely to converge to the "accurate" relative pose that best matches the feature correspondence. When we evaluate the self-supervised network, we use the poses at the start of exposure as the ground truth, to which the network does not learn to converge. But the effect of it is smaller than the "confusion" induced by the mismatch.

To verify the hypothesis above, we use the average of the poses of the start and the end of exposure as the pose of a blurry image and calculate the target relative pose from it. The results are marked with an asterisk and shown in Table III from the 2nd to the 4th row. "Table II 3(p)" denotes the average pooling version of the 3rd network of Table II. Similarly, the "(i)" denotes the bilinear interpolation version.

From the results, one can notice that all the self-supervised networks are more accurate. Besides, evaluated by the training set, the self-supervised networks are also slightly more accurate. The supervised networks trained with the new target pose have much higher accuracy compared to the old target pose calculated from the start time points of the images' exposure. We notice that the inlier rate drops when we use the new target pose. The reason is that the errors of the image pairs having less texture are more likely to be outliers because their neighbors have smaller errors. Obviously, the new target pose matches the feature correspondence better and acts as better supervision. But still, the remaining small mismatch makes it less good than self-supervised networks. So we believe that self-supervised learning is a better choice for the blurry image pairs that have an unknown relative pose perfectly matching the feature correspondence. This also provides us with the insight that taking the non-neglectable exposure duration of an image into account to refine its timestamp can benefit ego-motion estimation.

D. Networks for Tilt Angle Prediction

It is known that one can estimate the tilt of the camera relative to the plane in the view from the optical flow field [39]. Since tilt is a property of the flow field and hence affects both images, it cannot be estimated iteratively by our ICSTN-based framework that warps only one image (Fig. 2). For this preliminary investigation, we employ a single deep network block to predict tilt angles from a pair of derotated

images, supervised by ground truth. Shown in Table IV, the best network’s EPE’s standard deviation is around 4 degrees for both angles. Although the prediction is noisy, it may serve as an unbiased absolute information source to update the gyroscope integration. We leave this to further work.

TABLE IV
NETWORKS PREDICTING TILT ANGLES

Networks	Inlier Rate(%)	EPE’s Std. Dev. (radian, 1e-2)	Medians of EPE’s ABS (radian, 1e-2)
Table I 2*	97.13	(7.72, 6.57)	(5.06, 4.30)
Table I 3*	96.91	(8.71, 7.50)	(5.75, 4.87)

IV. EVALUATION

We use the 4th network of Table III for evaluation and comparison to traditional feature-based methods. We use MATLAB functions for feature detection and matching. Note that one can get more points by tuning the parameters of feature detection. Here we only show the results of the default parameters. If enough points are detected, 50 uniformly distributed ones are selected. The translation is obtained by calculating the similarity matrix (with known in-plane rotation, 3 degrees of freedom left) based on linear least squares and random sample consensus (RANSAC).

A. Simulated Dataset

We generate a dataset of 5000 image pairs with different exposure duration (ranges from 0.2ms to 20ms) and random distance-scaled velocity vectors having the same norm to compare the performance of the network and feature-based methods with increasing motion blur. Another dataset of 5000 sharp image pairs with different distance-scaled velocity vectors (same range as the training set) and the same exposure duration (0.2ms) is generated to study the effect of visual disparity. All the image pairs have random attitude and zero angular rates.

The norms of the estimated translations’ error vectors and their local standard deviations are shown in Fig. 4. We use linear fitting to show their trends. The local standard deviations are calculated with the window size of 10% of the total number of inliers. For feature-based methods, if there are less than 2 inlier matching in RANSAC, this pair is treated as an outlier. For the estimated pose, we apply the same local outlier rejection as Section III with the window size of 500. The final inlier rates of the network, SURF [40], ORB [11], and FAST [10] are shown in Fig. 4. The network has the highest inlier rates partly because it does not rely on the number of matches so it can perform prediction on every image pair. Fig. 4 shows that the network is most accurate with both datasets. Its performance is barely affected by the growing motion blur while feature-based methods more or less provide more noisy results. For the increasing disparity, the network is also least affected.

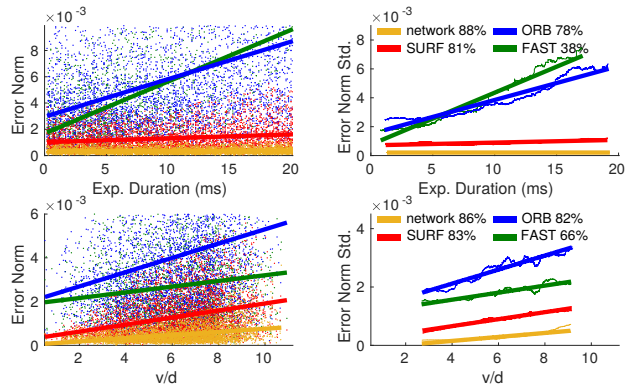


Fig. 4. Comparison between feature-based methods and the network. The top row shows how the norms of the error vectors of estimated translations and their local standard deviations change with increasing motion blur. The bottom row shows the effects of increasing visual disparity.

TABLE V
NETWORK AND SURF EVALUATED BY THE FLIGHT DATASET

Sequence	RMSE (1e-2): network / SURF (orig.) / SURF (hist. equal.)
1(0.3,1.3)	(2.10, <u>2.17</u> , <u>2.01</u>) / (1.95, <u>2.17</u> , 2.40) / (1.90 , 2.05 , 1.77)
2(0.6,2.5)	(4.21, 4.57, <u>3.65</u>) / (4.03, 4.35 , 3.70) / (3.91 , 4.36, 2.96)
3(1.2,3.2)	(<u>5.44</u> , 5.87, <u>5.03</u>) / (5.75, <u>5.48</u> , 6.36) / (5.20 , 5.25 , 4.34)
4(1.4,3.9)	(<u>10.2</u> , <u>9.48</u> , <u>10.0</u>) / (15.1, 11.5, 28.3) / (10.0 , 8.91 , 8.65)

B. Flight Data

We collect IMU measurements at 200Hz and monocular gray-scale images of size 320×240 pixels at 30Hz with the exposure duration of 20ms using an MYNT EYE D1000-120 visual-inertial sensor. The camera is downward-facing mounted on an Eachine Wizard X220 FPV Racing Drone carrying an NVIDIA Jetson TX2. The OptiTrack motion tracking system records the position and attitude of the MAV at 100Hz to calculate the ground-truth velocity. The images are undistorted and transformed to have the same size and intrinsic matrix as the training images. The camera’s attitude is estimated by the Madgwick filter [41] using the

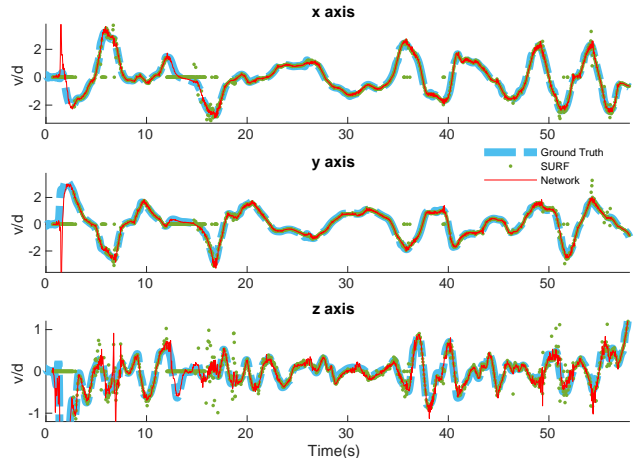


Fig. 5. The ratio of velocity to height of the number 4 flight sequence expressed in the world frame. Both methods use original images.

IMU measurements. We collected 4 one-minute sequences with increasing speed. Their average and maximum distance-scaled translational velocity are shown in Table V.

The results of the fastest sequence are shown in Fig. 5. SURF’s result is noisy in some parts of the flight mainly because of the big motion blur and scenes lacking texture. For 8.6% of image pairs, SURF has less than 2 inlier matching. We use zero vectors to show its results in this case. For the other 3 slower sequences, SURF has enough matches all the time. The root mean square errors (RMSEs) of the distance-scaled velocity are compared in Table V. When using original images, the network outperforms SURF more in faster sequences where fewer points are detected. In histogram equalized images, more SURF points are detected and the accuracy is slightly higher than the network. The network performs better on original images. We think it is because the images in the training set are without pre-processing.

V. CONCLUSION AND FUTURE WORKS

In this article, we have shown that CNNs are suitable for ego-motion estimation of fast-moving MAVs equipped with a downward-facing camera. When flying fast, both motion blur and visual disparity between subsequent images increase, which is handled better by a network than by traditional feature-based methods. Our investigation into the training of an ICSTN-based network shows that (1) it is better to take all blocks’ prediction errors into account, (2) a larger receptive field that can be achieved by pyramidal images allows to estimate larger motions, and (3) self-supervised learning based on the photometric error leads to better performance. For the next step, we will explore the uncertainty of the network’s prediction and build up a VIO system.

APPENDIX

A. Networks with Sharing Parameters among Blocks

Sharing parameters among the blocks of an ICSTN-based network is a way to widen the network (have more convolution kernels in each layer) without enlarging the model size. We train the 6th network of Table I and its variants in a self-supervised manner. The results are shown in Table VI. Besides sharing all the parameters we also try only sharing the fully-connected layer (FC).

The results show that sharing all the parameters and keeping the width of the network significantly reduce model size but hurt the accuracy a lot. The wider network having a slightly bigger model size fails to outperform the origin, either, shown in the 2nd row. Besides, it is slower (96Hz) than the original (101Hz). Sharing the fully-connected layer reduces the model size a little at the cost of the slight deterioration of accuracy.

We think when blocks have different parameters, the first block is trained to better handle bigger disparities and the last block focuses more on the smaller ones. Although sharing parameters widens the network, its enhancement to the model capacity of the block is less than the negative effects of weakening its specialization.

TABLE VI
NETWORKS WITH SHARED PARAMETERS

Share Params	Num. Params (original / wider)	EPE’s Approx. Normal Distr.: std(1e-4) (original / wider)
None	1.252M	(4.59, 4.04 , 5.94)
All	0.417M / 1.259M	(8.68, 8.42, 12.05) / (6.28, 5.96, 8.55)
FC	1.221M	(4.44 , 4.11, 6.02)

B. Error Distribution of Network’s Prediction

In order to better illustrate the performance of the networks, in Fig. 6 we show the error distribution of the 6th network of Table I trained in a self-supervised manner. Other networks’ error distribution figures have similar shapes. After the outlier rejection subscribed in Section II, its inlier rate is 85.2%. One can notice that the errors lie approximately unbiasedly close to zero. The prediction in the z -axis is noisier than the other 2 axes.

As shown in the left graph of Fig. 6, when the translation is bigger, the network has noisier predictions. It is also shown in Fig. 4, the uncertainty of prediction grows with motion. Note that the prediction error does not perfectly normally distribute, as shown in the right graph of Fig. 6. It is possible to train a deeper network with image pairs having even bigger motion to obtain error distribution closer to normal distribution. As for the current networks, when we fuse the network predictions with other sensors for state estimation, it would be better to adaptively adjust the uncertainty according to the prior knowledge of motion (from the dynamic model or IMU integration) or using another network to predict the uncertainty than using the approximately normal distribution. We leave this to future work.

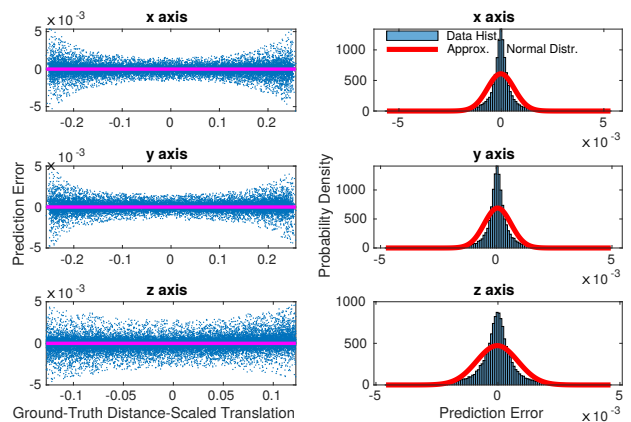


Fig. 6. Error distribution of the 6th network of Table I trained in the self-supervised manner. The inlier rate is 85.2%.

C. Evaluation of Tilt Prediction Networks by Flight Datasets

The evaluation results of the 1st network of Table IV by the sequence 4 of Table V is shown in Fig. 7. The noisy prediction follows the trend of ground truth to some extent but not good enough as an unbiased measurement.

Intuitively thinking, humans can better notice the tilt angles between the camera and the plane when there is bigger

translational motion. But from the evaluation results on the testing set and flight data, we failed to observe the relevance between the amount of motion and the accuracy of tilt prediction. During the training, the validation EPE started to increase slowly after 12 epochs, while for networks learning translational motion, the validation EPE keeps decreasing until around 23 epochs. So we think a better network architecture is required. Further study on this issue is required.

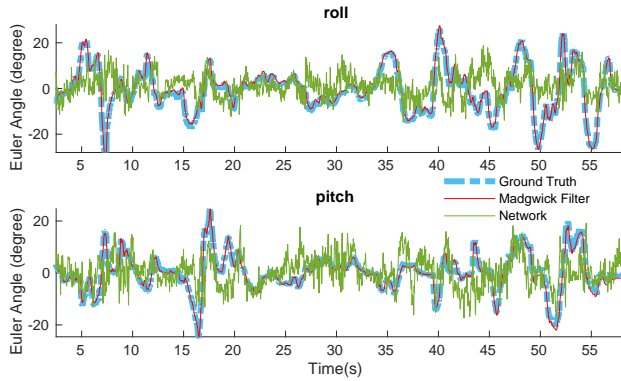


Fig. 7. Network’s prediction of the tilt angles evaluated with the number 4 flight sequence.

D. Networks with the Prior Pose as Input

In the previous parts of this article, the initial pose (shown in Fig. 2) of the network only contains the relative rotation. The translation is set to a zero vector. The network needs to deal with the whole visual disparity caused by translational motion. Because of the inertia of MAV, its translational velocity cannot change much during the sampling interval of the camera. So the translation vectors of temporally adjacent image pairs are similar. Here we add the predicted translation vector of the previous image pair as prior information to the initial pose. So the disparity of the image pair warped by the initial pose gets smaller. Here we call it the prior pose. It can improve accuracy because the network’s prediction is less noisy with smaller motion as shown in the left graph of Fig. 6.

TABLE VII
EVALUATION OF THE PRIOR POSE’S EFFECT ON ACCURACY

Network	RMSE (1e-2): Prior Input / Zero Input
Table III 4	(10.66, 9.59, 10.49) / (10.23, 9.48, 10.01)
Table II 5*	(16.92, 12.45, 24.73) / (16.52, 12.19, 24.43)

We evaluate 2 networks with number 4 flight sequence, as shown in Table VII. The networks having zero input are slightly more accurate. We think the reason for their similar performance is that the flight speed of the MAV is not very fast in our dataset. When the initial translation is a zero vector, the average absolute values of the difference between the network’s input initial translation and output are $3.29e-2$, $2.71e-2$, and $0.86e-2$ in 3 axes. The values drop to $2.83e-3$, $2.43e-3$, and $1.97e-3$ with the prior pose. The networks are

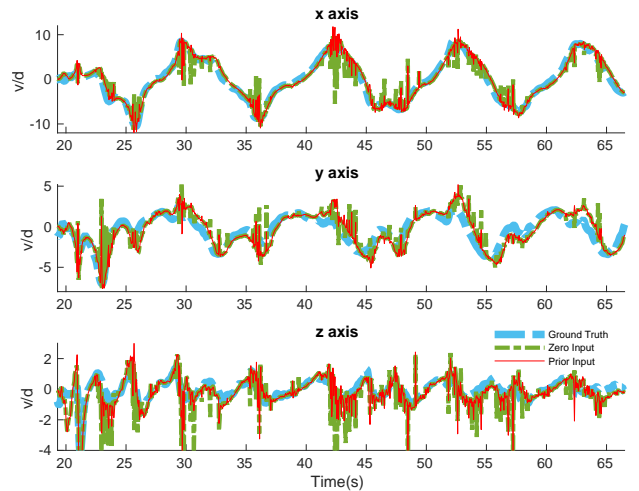


Fig. 8. The ratio of velocity to height expressed in the world frame. The network’s results with and without the prior pose are compared using the number 2 indoor 45-degree downward-facing sequence of the UZH-FPV dataset.

trained with a big range of motion that makes them capable enough for the whole disparity of image pairs in our flight dataset. The average predicted translation is smaller than the value (around 0.1) where the standard deviation starts to increase, as shown in Fig. 6. The effect of using the prior pose is further studied with faster flight in the next subsection.

E. Evaluation by Public Flight Dataset

We evaluate the 4th network of Table III with the 6 indoor 45-degree downward-facing flight sequences that have public ground truth from the UZH-FPV [42] dataset. For this dataset, the distance to the ground is unknown. So we manually set the initial distance at the starting point of the ground truth data to make the RMSE smaller. These sequences are faster than the flight sequence we collected. The maximum speed of each sequence and the networks’

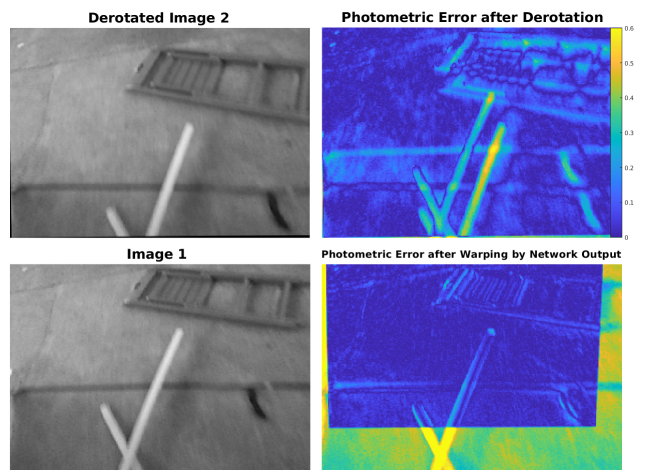


Fig. 9. The network’s performance when the scene is not a perfectly planar surface.

TABLE VIII
EVALUATION BY A PUBLIC DATASET OF FAST MAV FLIGHT

Sequence	RMSE (1e-1): Prior Input / Zero Input
2 (6.97m/s)	(10.76, 11.81, 7.53) / (14.48, 12.63, 8.70)
4 (6.55m/s)	(9.94, 14.64, 6.80) / (12.16, 14.77, 8.40)
9 (11.23m/s)	(9.70, 12.78, 10.55) / (21.15, 15.07, 15.77)
12 (4.33m/s)	(7.74, 8.44, 6.30) / (9.38, 8.85, 6.48)
13 (7.92m/s)	(9.86, 19.08, 6.56) / (14.18, 19.13, 8.50)
14 (9.54m/s)	(33.06, 22.27, 17.08) / (36.75, 21.21 , 21.37)

RMSEs are shown in Table VIII. Fig. 9 shows that the network’s performance when the scene is not a perfectly planar surface. The network is disturbed a little by the objects lying on the ground because of their rich visual textures. But since the objects are low enough for the MAV, the network can give a relatively accurate prediction. Note that there are many other scenes that are not inside a single plane. There are also high obstacles and strings. But since most of the time the ground plane takes up the majority of the image, the network outputs reasonable predictions. Another source of inaccuracy is that the attitude estimation from the Madgwick filter is less accurate because of the big acceleration during fast flight.

Now let’s revisit the prior pose. With the prior pose, the accuracy increases significantly and the prediction is less noisy, as shown in Table VIII and Fig. 8. We think the reason is that the visual disparities of the image pairs in the UZH-FPV dataset are big enough for the network’s accuracy to decrease. Take the number 9 sequence as an example, the average absolute values of the difference between the network’s input initial translation and output drop from $1.36e-1$, $9.51e-2$, and $6.46e-2$ to $2.14e-2$, $1.19e-2$, and $1.50e-2$ after involving the prior pose. From Fig. 10 one can clearly see the big disparity when the MAV flies at around 9.2m/s close to the ground. As shown in the 2nd column, without the prior pose, the network decreases the disparity a lot but still not enough. From the 3rd column, one can notice that the disparity is already small after the pre-warping by the prior pose, which is easier for the network. If other information sources like the IMU integration and rangefinder’s measurements are available, the prior pose can be more accurate so the network is less demanded to deal

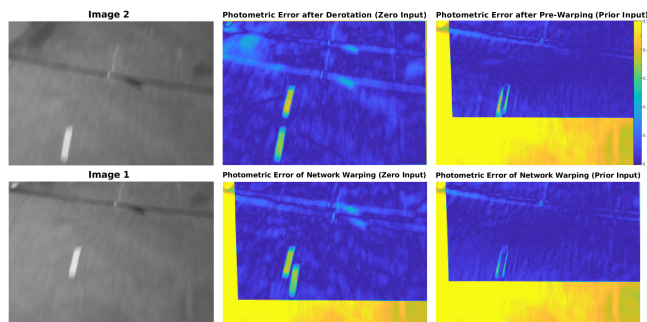


Fig. 10. Comparison between with and without the prior pose when the visual disparity is big.

with big visual disparity. Networks can be trained with image pairs that have smaller disparities to enhance their capability.

ACKNOWLEDGMENT

The authors would like to thank Nilay Y. Sheth for his supports in developing the quadrotor MAV with GPU and collecting the flight datasets.

REFERENCES

- [1] G. De Croon and C. De Wagter, “Challenges of autonomous flight in indoor environments,” in *2018 IEEE/RSJ International Conference on Intelligent Robots and Systems (IROS)*, pp. 1003–1009, IEEE, 2018.
- [2] C. Forster, M. Pizzoli, and D. Scaramuzza, “Svo: Fast semi-direct monocular visual odometry,” in *2014 IEEE international conference on robotics and automation (ICRA)*, pp. 15–22, IEEE, 2014.
- [3] R. Mur-Artal, J. M. M. Montiel, and J. D. Tardos, “Orb-slam: a versatile and accurate monocular slam system,” *IEEE transactions on robotics*, vol. 31, no. 5, pp. 1147–1163, 2015.
- [4] M. Li and A. I. Mourikis, “High-precision, consistent ekf-based visual-inertial odometry,” *The International Journal of Robotics Research*, vol. 32, no. 6, pp. 690–711, 2013.
- [5] M. Bloesch, S. Omari, M. Hutter, and R. Siegwart, “Robust visual inertial odometry using a direct ekf-based approach,” in *2015 IEEE/RSJ international conference on intelligent robots and systems (IROS)*, pp. 298–304, IEEE, 2015.
- [6] T. Qin, P. Li, and S. Shen, “Vins-mono: A robust and versatile monocular visual-inertial state estimator,” *IEEE Transactions on Robotics*, vol. 34, no. 4, pp. 1004–1020, 2018.
- [7] K. Sun, K. Mohta, B. Pfrommer, M. Watterson, S. Liu, Y. Mulgaonkar, C. J. Taylor, and V. Kumar, “Robust stereo visual inertial odometry for fast autonomous flight,” *IEEE Robotics and Automation Letters*, vol. 3, no. 2, pp. 965–972, 2018.
- [8] C. Campos, R. Elvira, J. J. G. Rodríguez, J. M. Montiel, and J. D. Tardós, “Orb-slam3: An accurate open-source library for visual, visual-inertial and multi-map slam,” *arXiv preprint arXiv:2007.11898*, 2020.
- [9] J. Shi *et al.*, “Good features to track,” in *1994 Proceedings of IEEE conference on computer vision and pattern recognition*, pp. 593–600, IEEE, 1994.
- [10] M. Trajковиć and M. Hedley, “Fast corner detection,” *Image and vision computing*, vol. 16, no. 2, pp. 75–87, 1998.
- [11] E. Rublee, V. Rabaud, K. Konolige, and G. Bradski, “Orb: An efficient alternative to sift or surf,” in *2011 International conference on computer vision*, pp. 2564–2571, Ieee, 2011.
- [12] P. Foehn, D. Brescianini, E. Kaufmann, T. Cieslewski, M. Gehrig, M. Muglikar, and D. Scaramuzza, “Alphapilot: Autonomous drone racing,” *arXiv preprint arXiv:2005.12813*, 2020.
- [13] S. Zhong and P. Chirarattananon, “Direct visual-inertial ego-motion estimation via iterated extended kalman filter,” *IEEE Robotics and Automation Letters*, vol. 5, no. 2, pp. 1476–1483, 2020.
- [14] G. Costante, M. Mancini, P. Valigi, and T. A. Ciarfuglia, “Exploring representation learning with cnns for frame-to-frame ego-motion estimation,” *IEEE robotics and automation letters*, vol. 1, no. 1, pp. 18–25, 2015.
- [15] I. Melekhov, J. Ylioinas, J. Kannala, and E. Rahtu, “Relative camera pose estimation using convolutional neural networks,” in *International Conference on Advanced Concepts for Intelligent Vision Systems*, pp. 675–687, Springer, 2017.
- [16] S. Wang, R. Clark, H. Wen, and N. Trigoni, “End-to-end, sequence-to-sequence probabilistic visual odometry through deep neural networks,” *The International Journal of Robotics Research*, vol. 37, no. 4-5, pp. 513–542, 2018.
- [17] T. Zhou, M. Brown, N. Snavely, and D. G. Lowe, “Unsupervised learning of depth and ego-motion from video,” in *Proceedings of the IEEE Conference on Computer Vision and Pattern Recognition*, pp. 1851–1858, 2017.
- [18] R. Li, S. Wang, Z. Long, and D. Gu, “Undeepvo: Monocular visual odometry through unsupervised deep learning,” in *2018 IEEE international conference on robotics and automation (ICRA)*, pp. 7286–7291, IEEE, 2018.

- [19] A. Ranjan, V. Jampani, L. Balles, K. Kim, D. Sun, J. Wulff, and M. J. Black, "Competitive collaboration: Joint unsupervised learning of depth, camera motion, optical flow and motion segmentation," in *Proceedings of the IEEE Conference on Computer Vision and Pattern Recognition*, pp. 12240–12249, 2019.
- [20] Y. Chen, C. Schmid, and C. Sminchisescu, "Self-supervised learning with geometric constraints in monocular video: Connecting flow, depth, and camera," in *Proceedings of the IEEE International Conference on Computer Vision*, pp. 7063–7072, 2019.
- [21] J. Bian, Z. Li, N. Wang, H. Zhan, C. Shen, M.-M. Cheng, and I. Reid, "Unsupervised scale-consistent depth and ego-motion learning from monocular video," in *Advances in Neural Information Processing Systems*, pp. 35–45, 2019.
- [22] A. Geiger, P. Lenz, and R. Urtasun, "Are we ready for autonomous driving? the kitti vision benchmark suite," in *2012 IEEE Conference on Computer Vision and Pattern Recognition*, pp. 3354–3361, IEEE, 2012.
- [23] M. Burri, J. Nikolic, P. Gohl, T. Schneider, J. Rehder, S. Omari, M. W. Achtelik, and R. Siegwart, "The euroc micro aerial vehicle datasets," *The International Journal of Robotics Research*, vol. 35, no. 10, pp. 1157–1163, 2016.
- [24] N. J. Sanket, C. D. Singh, C. Fermüller, and Y. Aloimonos, "Prgflow: Benchmarking swap-aware unified deep visual inertial odometry," *arXiv preprint arXiv:2006.06753*, 2020.
- [25] O. D. Faugeras and F. Lustman, "Motion and structure from motion in a piecewise planar environment," *International Journal of Pattern Recognition and Artificial Intelligence*, vol. 2, no. 03, pp. 485–508, 1988.
- [26] C.-H. Lin and S. Lucey, "Inverse compositional spatial transformer networks," in *Proceedings of the IEEE Conference on Computer Vision and Pattern Recognition*, pp. 2568–2576, 2017.
- [27] M. Jaderberg, K. Simonyan, A. Zisserman, *et al.*, "Spatial transformer networks," in *Advances in neural information processing systems*, pp. 2017–2025, 2015.
- [28] D. Sun, S. Roth, and M. J. Black, "A quantitative analysis of current practices in optical flow estimation and the principles behind them," *International Journal of Computer Vision*, vol. 106, no. 2, pp. 115–137, 2014.
- [29] A. Paszke, S. Gross, F. Massa, A. Lerer, J. Bradbury, G. Chanan, T. Killeen, Z. Lin, N. Gimelshein, L. Antiga, *et al.*, "Pytorch: An imperative style, high-performance deep learning library," in *Advances in neural information processing systems*, pp. 8026–8037, 2019.
- [30] D. P. Kingma and J. Ba, "Adam: A method for stochastic optimization," *arXiv preprint arXiv:1412.6980*, 2014.
- [31] X. Glorot and Y. Bengio, "Understanding the difficulty of training deep feedforward neural networks," in *Proceedings of the thirteenth international conference on artificial intelligence and statistics*, pp. 249–256, 2010.
- [32] T.-Y. Lin, M. Maire, S. Belongie, J. Hays, P. Perona, D. Ramanan, P. Dollár, and C. L. Zitnick, "Microsoft coco: Common objects in context," in *European conference on computer vision*, pp. 740–755, Springer, 2014.
- [33] A. Kendall, M. Grimes, and R. Cipolla, "Posenet: A convolutional network for real-time 6-dof camera relocalization," in *Proceedings of the IEEE international conference on computer vision*, pp. 2938–2946, 2015.
- [34] G. Huang, Z. Liu, L. Van Der Maaten, and K. Q. Weinberger, "Densely connected convolutional networks," in *Proceedings of the IEEE conference on computer vision and pattern recognition*, pp. 4700–4708, 2017.
- [35] K. He, X. Zhang, S. Ren, and J. Sun, "Identity mappings in deep residual networks," in *European conference on computer vision*, pp. 630–645, Springer, 2016.
- [36] D. Sun, X. Yang, M.-Y. Liu, and J. Kautz, "Pwc-net: Cnns for optical flow using pyramid, warping, and cost volume," in *Proceedings of the IEEE conference on computer vision and pattern recognition*, pp. 8934–8943, 2018.
- [37] Y. Xu, T. Xiao, J. Zhang, K. Yang, and Z. Zhang, "Scale-invariant convolutional neural networks," *arXiv preprint arXiv:1411.6369*, 2014.
- [38] N. Van Noord and E. Postma, "Learning scale-variant and scale-invariant features for deep image classification," *Pattern Recognition*, vol. 61, pp. 583–592, 2017.
- [39] G. De Croon, H. Ho, C. De Wagter, E. Van Kampen, B. Remes, and Q. Chu, "Optic-flow based slope estimation for autonomous landing," *International Journal of Micro Air Vehicles*, vol. 5, no. 4, pp. 287–297, 2013.
- [40] H. Bay, T. Tuytelaars, and L. Van Gool, "Surf: Speeded up robust features," in *European conference on computer vision*, pp. 404–417, Springer, 2006.
- [41] S. O. Madgwick, A. J. Harrison, and R. Vaidyanathan, "Estimation of imu and mag orientation using a gradient descent algorithm," in *2011 IEEE international conference on rehabilitation robotics*, pp. 1–7, IEEE, 2011.
- [42] J. Delmerico, T. Cieslewski, H. Rebecq, M. Faessler, and D. Scaramuzza, "Are we ready for autonomous drone racing? the uzh-fpv drone racing dataset," in *2019 International Conference on Robotics and Automation (ICRA)*, pp. 6713–6719, IEEE, 2019.